PHYSICAL REVIEW B **95**, 125123 (2017)

Hole-doping-induced melting of spin-state ordering in $PrBaCo_2O_{5.5+x}$

Ping Miao,[1,2,*] Xiaohuan Lin,[3] Sanghyun Lee,[1] Yoshihisa Ishikawa,[1] Shuki Torii,[1] Masao Yonemura,[1,2] Tetsuro Ueno,[1,4]
Nobuhito Inami,[1] Kanta Ono,[1,2] Yingxia Wang,[3] and Takashi Kamiyama[1,2,†]
[1]*Institute of Materials Structure Science, High Energy Accelerator Research Organization (KEK), Tokai 319-1106, Japan*
[2]*Sokendai (The Graduate University for Advanced Studies), Tokai 319-1106, Japan*
[3]*College of Chemistry and Molecular Engineering, Peking University, Beijing 100871, China*
[4]*National Institute for Materials Science, Tsukuba, Ibaraki 305-0047, Japan*

(Received 20 December 2016; revised manuscript received 13 February 2017; published 20 March 2017)

The layered perovskite cobaltite $RBaCo_2O_{5.5}$ (R: rare-earth elements) exhibits an abrupt temperature-induced metal-insulator transition (MIT) that has been attributed to spin-state ordering (SSO) of Co^{3+} ions. Here we investigate the hole-doping member of $PrBaCo_2O_{5.5+x}$ ($0 \leqslant x \leqslant 0.24$) with multiple techniques. The analysis of crystal and magnetic structures by electron and neutron diffraction confirm the SSO in the insulating phase of undoped $PrBaCo_2O_{5.5}$, which is melted by increasing the temperature across the MIT. In addition, we discover that hole doping to $PrBaCo_2O_{5.5}$ also melts the SSO in conjunction with an insulator-metal transition. The experimental results from electron and neutron diffraction and soft-x-ray absorption spectroscopy (XAS) all lead to the conclusion that hole-doping-induced MIT occurs in the same manner as the temperature-induced MIT. Therefore, we propose a unified mechanism that dominates the temperature- and hole-doping-induced MIT in the $PrBaCo_2O_{5.5+x}$ system. Specifically, this mechanism involves symmetry breaking coupled with a SSO in the paramagnetic phase.

DOI: 10.1103/PhysRevB.95.125123

I. INTRODUCTION

The metal-insulator transition (MIT) is observed in many transition-metal oxides and manifests itself by large change in resistivity across a phase boundary. Interplay between the spin, charge, orbital, and lattice degrees of freedom has been found to play a crucial role in developing various electronic phases that span both the metallic and insulating sides; e.g., ferromagnetic metals, antiferromagnetic metals, Mott–Hubbard insulators, and charge-transfer insulators [1,2]. Recently, another type of degree of freedom has attracted much attention for its effects on the magnetic and transport properties of iron-based superconductors [3–5]. It is referred to as the spin-state degree of freedom (SSDF) and describes the distribution of d electronic spins over the crystal-field-split t_{2g} and e_g orbitals.

Although the SSDF is present in many d-electron systems, how it correlates with the properties of materials is still not well understood. $LaCoO_3$ has been known to be a prototypic system for exhibiting different spin states of the trivalent cobalt atoms through three kinds of configuration of $3d^6$ electrons: low-spin (LS, $t_{2g}^6 e_g^0$, $S = 0$), intermediate-spin (IS, $t_{2g}^5 e_g^1$, $S = 1$) and high-spin (HS, $t_{2g}^4 e_g^2$, $S = 2$) states. Upon increasing the temperature to around 100 K, it undergoes a spin-state transition (SST) in which the nonmagnetic LS ground state transforms to a paramagnetic (PM) higher spin state, although whether this PM susceptibility stems from a HS or IS state is still debated [2,6–8]. Goodenough *et al.* [9,10] postulated that a long-range ordering of LS and HS Co ions, which is called spin-state ordering (SSO) (not to be confused with the ordering of magnetic moments in traditional magnetically ordered structures), accompanies the SST and elucidates the magnetic and charge-transport properties. To be noted, SST is defined by a change of spin states, so it is not necessarily accompanied by SSO, whereas SSO always occurs together with a SST. However, static ordering of LS and HS (or IS) ions in bulk $LaCoO_3$ has never been found experimentally [10–14]. On the other hand, Korotin *et al.* [15] demonstrated by local density approximation + U (LDA + U) calculations that the IS state is almost degenerate with the LS ground state and lower in energy than the HS state. This IS scenario has been popular until recently when several theoretical studies [7,16–19] revived the HS scenario in terms of the dynamically or statically mixed LS or HS state, which is corroborated by the result from x-ray absorption spectroscopy [20]. However, the latest inelastic x-ray scattering (IXS) and infrared spectroscopy experiments [21] indicate a complex spin-state disproportionation including all the LS, IS, and HS states.

Much attention has been paid to an analogous cobaltite family, $RBaCo_2O_{5.5}$ (R = Nd [22], Gd [23], Tb [24], Dy [25], Ho [26], and Y [27–29]) with the nominal valence of the Co ion being +3 because a long-range SSO has been found to occur in conjunction with a temperature-induced (TI) MIT. The poor metallic phase (we refer to "poor metallic phase" as the phase above the transition temperature T_{MI} or the transition hole-doping level x_{MI}, despite the temperature dependence of resistivity of the "poor metallic phase" actually still behaving like a semiconductor) of $RBaCo_2O_{5.5}$ crystalizes into an orthorhombic crystal structure (space group $Pmmm$) with a unit cell $a_p \times 2a_p \times 2a_p$, where a_p is the lattice parameter of the pseudocubic perovskite ABO_3 subcell [30–32]; see Fig. 1(a). The ordered distribution of oxygen vacancies in the PrO_x layer results in an alternative arrangement of corner-sharing CoO_5 pyramids (Pyr) and CoO_6 octahedra (Oct) along the b axis, leading to two nonequivalent crystallographic sites labeled Co(Pyr) and Co(Oct). Some of the early studies [31,32]

---

[*] Present address: Department of Physics & Astronomy, Texas A&M University, College Station 77843, USA; miao@post.kek.jp

[†] takashi.kamiyama@kek.jp

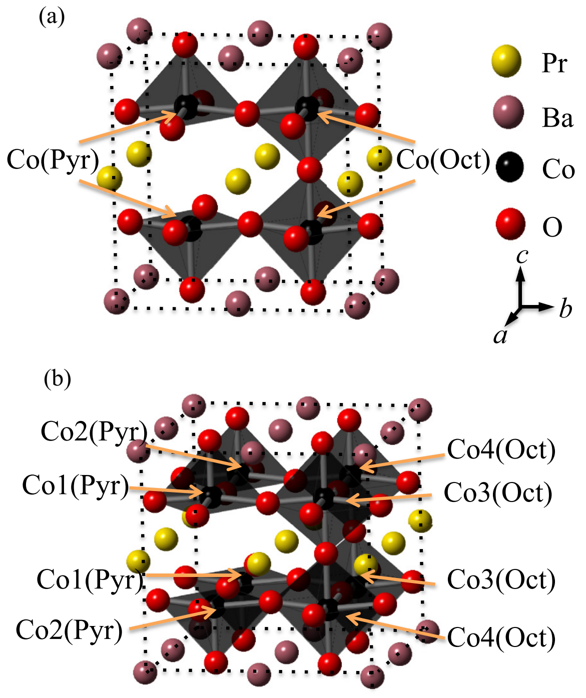

FIG. 1. (a) $Pmmm(a_p \times 2a_p \times 2a_p)$ crystal unit cell with oxygen vacancy in the PrO_x layer leading to ordering along the b axis. The crystal structure consists of two nonequivalent crystallographic Co sites: one pyramidal site Co(Pyr) and one octahedral site Co(Oct). (b) $Pmma(2a_p \times 2a_p \times 2a_p)$ crystal unit cell with four nonequivalent crystallographic Co sites labeled Co1(Pyr), Co2(Pyr), Co3(Oct), and Co4(Oct).

asserted that the $Pmmm(a_p \times 2a_p \times 2a_p)$ structure survives when the material undergoes a TI-MIT into the insulating state. Later, Chernenkov *et al.* [23] used single-crystal x-ray diffraction to reveal superlattice reflections along the a axis below T_{MI}, which are absent in the poor-metallic phase in $GdBaCo_2O_{5.5}$, and thus concluded that the insulating phase consists of a different orthorhombic structure $Pmma(2a_p \times 2a_p \times 2a_p)$ with four Co sites: Co1(Pyr), Co2(Pyr), Co3(Oct), and Co4(Oct) [see Fig. 1(b)]. They attributed the splitting of two sites of $Pmmm$ structure into four sites of $Pmma$ structure the SSO. Followup works corroborated this model and assigned the specific spin states of these four sites by assessing the individual magnetic moment of the Co^{3+} ions with the magnetic structures analyzed from neutron powder diffraction [24,26,27,33,34].

A similar drop in resistivity that occurs as a function of hole-doping fraction x was found in the high-temperature region of the resistivity curve of single-crystal $GdBaCo_2O_{5.5+x}$ [35] and thin films of $LnBaCo_2O_{5.5+x}$ (Ln = Er, Pr) [36], which we hereafter refer to as the hole-doping-induced metal-insulator transition (HDI-MIT). However, no reports have discussed the hole-doping effect on the spin states involving Co^{3+} ions or the relationship between the HDI-MIT and the TI-MIT of the $RBaCo_2O_{5.5+x}$ system, partly because of lack of consensus on the detailed crystal and magnetic structures of $RBaCo_2O_{5.5+x}$ ($x \geqslant 0$) [23–27,30–32,37,38]. To resolve this situation, we took advantage of the fact that $PrBaCo_2O_{5.5+x}$ can reach the highest hole-doping level ($0 \leqslant x \leqslant 0.24$) within the rare-earth family and carried out a multiprobe study (neutron, electron, and x-rays) on the crystal and Co-ion spin and orbital structures and characterized the transport and magnetic properties of a full series of polycrystalline samples.

II. EXPERIMENTAL METHOD

$PrBaCo_2O_{5.5+x}$ polycrystalline samples were synthesized by the solid-state reaction method with a combined ethylenediaminetetraacetic acid (EDTA)-citrate complex sol-gel process [39,40]. The hole-doping fraction x was controlled by annealing the as-prepared samples in a pure nitrogen atmosphere at various temperatures with the nominal x ranging from 0 to 0.24. The fraction x was determined by both iodometric titration and neutron powder diffraction, with the results agreeing with each other within the error of ~0.02. The high-resolution neutron powder diffraction measurements were performed by using SuperHRPD at Japan Proton Accelerator Research Complex (J-PARC). The best resolution is $\frac{\Delta d}{d} = 0.035\%$ at $2\theta = 172^\circ$. We used the software SARAH [41] to carry out the representation analysis on magnetic structure. Rietveld refinement was performed using the software Z-RIETVELD [42,43] and FULLPROF [44], and the residual values R_{wp} and R_M were both below 10%. The electron diffraction pattern was acquired on a JEOL JEM-2100 transmission electron microscope with an accelerating voltage of 200 kV and a camera length of 150 cm, giving a point resolution of 2.3 Å. Soft-x-ray absorption spectroscopy (XAS) was carried out at the BL-16A beamline of the Photon Factory at the High Energy Accelerator Research Organization (KEK), Japan. Samples were mounted in a liquid-He cryostat and XAS spectra were obtained in total electron yield (TEY) mode. The resistivity was measured by using a standard dc four-probe method on a Quantum Design physical property measurement system (PPMS), and the magnetization was measured by using a dc superconducting quantum interference device (SQUID) magnetometer (MPMS) at the Cross–Tokai user laboratories.

III. RESULTS

A. Temperature-induced metal-insulator transition and hole-doping-induced metal-insulator transition

In the undoped member, $PrBaCo_2O_{5.5}$, the TI-MIT occurring in the paramagnetic (PM) phase can be identified by a sharp drop in resistivity ρ around $T_{\mathrm{MI}} = 350$ K, which corresponds to the transition from an insulator to a poor metal [see Fig. 2(a)]. The change of slope of the inverse magnetic susceptibility in the PM phase in Fig. 2(a) corresponds to the Curie–Weiss effective magnetic moments $\mu_{\mathrm{eff}} = 2.50(1)\mu_B$ and $5.39(1)\mu_B$ below and above T_{MI}, respectively. It is hard to estimate the contribution of a Pr^{3+} ion to the effective magnetic moment because there might be an exchange interaction between Pr^{3+} and Co^{3+} ions. However, it is not unreasonable to assume that the Pr^{3+} has the same (or very similar) contribution both above and below T_{MI} so that such a significant difference in μ_{eff} indicates the SST of the Co^{3+} ions. HDI-MIT executes a similar drop more than two order of magnitude in resistivity that occurs as a function of hole-doping fraction x [see ρ vs x in Fig. 2(b)].

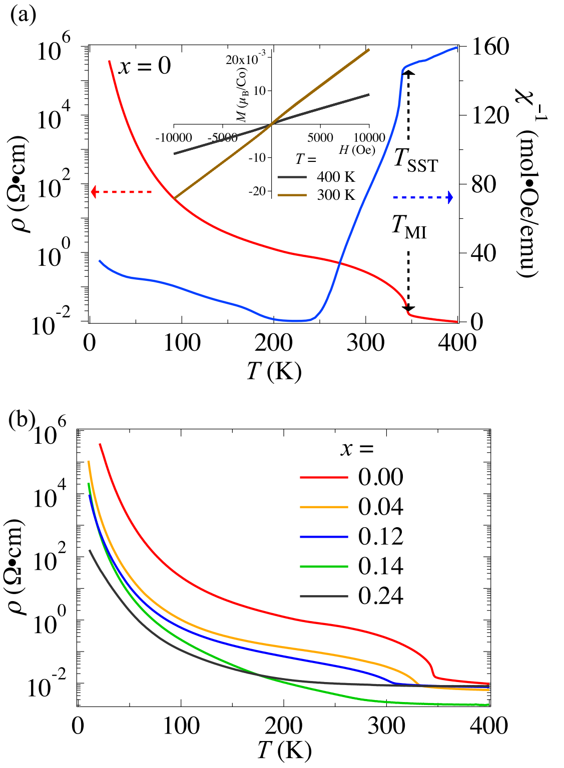

FIG. 2. (a) Resistivity ρ and inverse magnetic susceptibility χ^{-1} as a function of temperature for samples with $x = 0$. The abrupt changes in ρ and χ^{-1} at T_{MI} mark the concurrence of the SST and MIT. The susceptibility was measured in the 100 Oe field after zero-field cooling (ZFC). The inset shows the isothermal magnetization as a function of magnetic field (M-H curve) measured at 300 and 400 K, respectively, from which the paramagnetic behavior is made evident at both temperatures. So the MIT occurs in the paramagnetic phase. (b) Resistivity ρ as a function of temperature for various hole-doping fractions x, which shows a sharp drop with increasing hole doping. The x dependence of ρ reveals a HDI-MIT at $x = 0.12$. The anomalously low value in ρ for $x = 0.14$ above ∼200 K is possibly due to the lower boundary resistance of polycrystalline grains compared with that in samples with other hole-doping fractions. This speculation can be verified by the resistivity as a function of x in single crystals of $\mathrm{GdBaCo_2O_{5.5+\mathit{x}}}$ [35].

B. Crystal and magnetic structures of $\mathrm{PrBaCo_2O_{5.5}}$

Although the SSO model has been well established in $R\mathrm{BaCo_2O_{5.5}}$ ($R =$ Nd [22], Gd [23], Tb [24], Dy [25], Ho [26], and Y [27–29]), there is no report on this model for undoped $\mathrm{PrBaCo_2O_{5.5}}$. We first study the crystal structure and the related magnetic structure of $\mathrm{PrBaCo_2O_{5.5}}$ to verify the SSO in this compound. Since this article focuses on the hole-doping effect, the details of undoped $\mathrm{PrBaCo_2O_{5.5}}$ are not elaborately discussed in the main text but instead are attached in Appendix A.

Both electron diffraction and high-resolution neutron powder diffraction (NPD) provide corroborative evidence that the crystal structure of $\mathrm{PrBaCo_2O_{5.5}}$ undergoes a first-order phase transition from high-temperature $Pmmm(a_p \times 2a_p \times 2a_p)$ [Fig. 1(a)] to low-temperature $Pmma(2a_p \times 2a_p \times 2a_p)$ [Fig. 1(b)] across T_{MI}. In the $Pmma$ phase, two magnetic phase transitions occur subsequently at T_{N1} and T_{N2} [see Fig. 3(a)], with the corresponding magnetic structures shown in Fig. 3(b). The relative difference in the magnitudes of moments indicate the spin-state configuration of the HS state for Co1(Pyr), the IS state for Co2(Pyr) and Co4(Oct), and the LS state for Co3(Oct). Alternatively, the different moments can be attributed to the spin-state disproportionation; namely, each Co site resides in a HS or LS mixed state and the ratio of HS to LS differs among the four sites. The analysis on the average Co–O bond lengths below T_{MI} leads to a similar conclusion. Therefore, a long-range SSO is identified in the low-temperature $Pmma$ phase. The spin-state configuration in the high-temperature $Pmmm$ phase cannot be directly determined because there is no magnetic-ordered phase nearby in phase space. However, the Co–O bond length of the undoped sample and the analysis of the magnetic structure of the hole-doping sample below will shed light on the spin states in this phase. We conclude that, in $\mathrm{PrBaCo_2O_{5.5}}$, the crystal structure change from $Pmma$ to $Pmmm$ corresponds to the melting of SSO, identical to the other rare-earth families, $R\mathrm{BaCo_2O_{5.5}}$ ($R =$ Nd [22], Gd [23], Tb [24], Dy [25], Ho [26], and Y [27–29]).

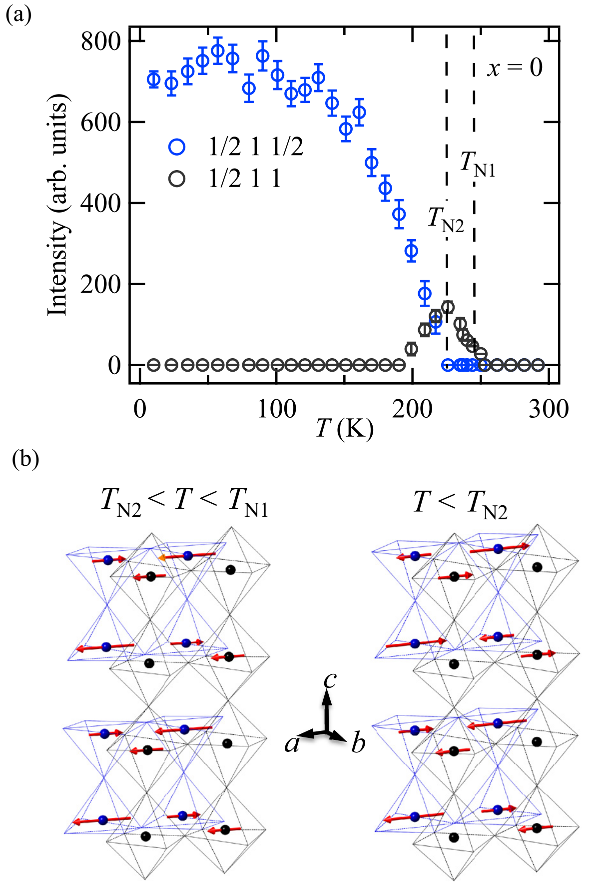

FIG. 3. (a) Integrated intensity as a function of temperature for magnetic reflections 111 and $11\frac{1}{2}$ indexed by the unit cell $(2a_p \times 2a_p \times 2a_p)$ from neutron powder diffraction. (b) Ferrimagnetic ($T_{N2} \leqslant T \leqslant T_{N1}$) structure of phase 1 and antiferromagnetic ($T \leqslant T_{N2}$) structures of phase 2. Octahedra are in black and pyramids in blue.

TABLE I. The atomic occupancy, coordinates, and isotropic displacement parameters for $x = 0.24$ sample obtained from Rietveld refinement of neutron powder diffraction data at 300 K. The refinement is performed by using the orthorhombic $Pmmm(a_p \times 2a_p \times 2a_p)$ structure. The lattice parameters and criteria of the refinement quality are $a = 3.89832(1)$ Å, b=7.90892(2) Å, c=7.64649(2) Å, R_{wp}=6.83%.

Atom	Site	Occupancy	x	y	z	$100U_{iso}$(Å^2)
Ba	$2o$	1	0.5	0.2507(1)	0	0.09(2)
Pr	$2p$	1	0.5	0.2654(1)	0.5	0.56(3)
Co1	$2r$	1	0	0.5	0.2494(2)	0.49(3)
Co2	$2q$	1	0	0	0.2524(2)	0.41(4)
O1	$1a$	1	0	0	0	1.25(3)
O2	$1e$	1	0	0.5	0	0.84(3)
O3	$1g$	0.813(5)	0	0.5	0.5	0.45(4)
O4	$1c$	0.652(6)	0	0	0.5	1.11(4)
O5	$2s$	1	0.5	0	0.2874(2)	1.39(2)
O6	$2t$	1	0.5	0.5	0.2715(2)	1.18(2)
O7	$4u$	1	0	0.2484(1)	0.2763(1)	1.45(2)

C. Crystal and magnetic structures of $PrBaCo_2O_{5.5+x}$ ($x > 0$)

Next we discuss the HDI-MIT in the $0 < x \leqslant 0.24$ samples, which covers the transformation at $x = 0.12$ from the insulting phase to the poor-metallic phase [see inset of Fig. 2(b)]. The insulating side of the HDI-MIT starts at the stoichiometric end member $PrBaCo_2O_{5.5}$ with the $Pmma(2a_p \times 2a_p \times 2a_p)$ structure. Hole doping introduces oxygen ions into the empty site (pyramid) of in RO_x layer, as shown in Fig. 1(b). The inset of Fig. 4(b) shows the integrated intensity of the (131) neutron powder diffraction peak at 300 K, which declines as a function of hole-doping fraction x, reflecting a decreasing contribution from the $Pmma(2a_p \times 2a_p \times 2a_p)$ structure. The intensity finally vanishes at $x = 0.12$, which indicates a structural phase transition. Previous studies [35,45] asserted that, for $x > 0.1$, $RBaCo_2O_{5.5+x}$ crystallizes into the tetragonal $P4/mmm(a_p \times a_p \times 2a_p)$ structure with only one nonequivalent crystallographic site forthe Co ion, corresponding to the partial and random distribution of oxygen vacancies in the RO_x layer [see Fig. 4(a)]. However, Fig. 4(b) shows that we see the 040 and 400 reflections, whose positions are directly related to the lattice constants a and b, remain separate until $x = 0.14$, unambiguously suggesting that the structure transforms into orthorhombic $Pmmm(a_p \times 2a_p \times 2a_p)$, which corresponds to the disproportionate distribution of oxygen vacancies in PrO_x layer [i.e., oxygen ions prefer the right site to the left one in Fig. 1(a)]. Although the 040 and 400 reflections seem to merge into a single peak in Fig. 4(b) at $x = 0.24$, the ratio of full width at half maximum (FWHM) to the d spacing is 0.25%, which is broader than the other single peak [$\frac{\text{FWHM}}{d} \approx 0.17\%$; see Fig. 4(c)], indicating an orthorhombic distortion. Additional evidence for the $Pmmm(a_p \times 2a_p \times 2a_p)$ structure at $x = 0.24$ is provided by both neutron and electron diffraction, in which superlattice reflections along the b axis with respect to the $(a_p \times a_p \times 2a_p)$ unit cell are observed [see Figs. 4(d) and 4(e), respectively]. The results from Rietveld refinement are given in Table I. Therefore, we conclude that the crystal structure phase transition across the HDI-MIT is from $Pmmm(a_p \times 2a_p \times 2a_p)$ to $Pmma(2a_p \times 2a_p \times 2a_p)$, which is identical to that across the TI-MIT.

We also analyzed the magnetic structure of the $x = 0.24$ sample to infer the spin states of Co^{3+} ions at higher temperatures because the HDI-MIT also occurs in the PM phase [see Fig. 4(f)]. Our synchrotron XRD experiment reveals that the $Pmmm$ structure is preserved at temperatures down to about 30 K. As shown in Fig. 4(f), the magnetic-ordering phase with propagation vector $\boldsymbol{k}_m = (\frac{1}{2},0,0)$ can be identified in the neutron-diffraction pattern by the appearance of the $(\frac{1}{2}11)$ magnetic reflection at $T_N = 120$ K, whose intensity gradually increases with decreasing temperature. According to Landau theory, the magnetic ordering from such a second-order phase transition will involve a single irreducible representation (IR). Therefore, given the $Pmmm$ crystal structure with $\boldsymbol{k}_m = (\frac{1}{2},0,0)$, representation analysis allows us to determine the possible IRs and the corresponding basis vectors (BVs) for the magnetic structure. Through Rietveld refinement, we find the G-type antiferromagnetic structure with the Co-ion spins pointing along either the a axis or the b axis, as shown in Fig. 4(f), and the magnitude of magnetic moment M at 11 K is determined to be about $1.3\mu_B$. The details about the representation analysis and Rietveld refinement are included in Appendix B.

The x-ray absorption spectroscopy studies by Medling *et al.* [46,47] indicate that, in $La_{1-x}Sr_xCoO_3$, the doping-induced holes are nearly equally distributed over the Co and O atoms, resulting in coexistence of the Co^{4+} ions and the magnetic O^- ions. Accordingly, we expect the $x = 0.24$ sample contains statistically 12% Co^{4+} ions and 12% magnetic O^- ions. Since 12% of Co^{4+} ions ($S = \frac{1}{2}$, $t_{2g}^5 e_g^0$) and 12% of O^- ions ($S = \frac{1}{2}$) contribute at most μ_B to M, the major component must come from the Co^{3+} ions; namely, the Co^{3+} ions in the two Co sites of the $Pmmm(a_p \times 2a_p \times 2a_p)$ structure are all in IS ($S = 1$, $t_{2g}^4 e_g^2$) states. Comparing with the spin-state configuration in the $Pmma(2a_p \times 2a_p \times 2a_p)$ structure at $x = 0$, we see that, by increasing the hole-doping fraction x, the LS and HS Co^{3+} ions undergo the SST into the IS state so that the SSO in the $Pmma$ model is melted. Further evidence supporting this conclusion is a jump in the Curie–Weiss effective magnetic moment μ_{eff} from $2.52(1)\mu_B$ ($x = 0.04$) to $3.24(1)\mu_B$ ($x = 0.12$), as shown in Fig. 5.

Because only 8% increase in the total number of Co^{4+} and O^- ions cannot account for the $0.72\mu_B$ difference, some of the Co^{3+} ions must convert from the LS to IS state. As a result, the hole doing to $PrBaCo_2O_{5.5}$ induces the SST, resulting in

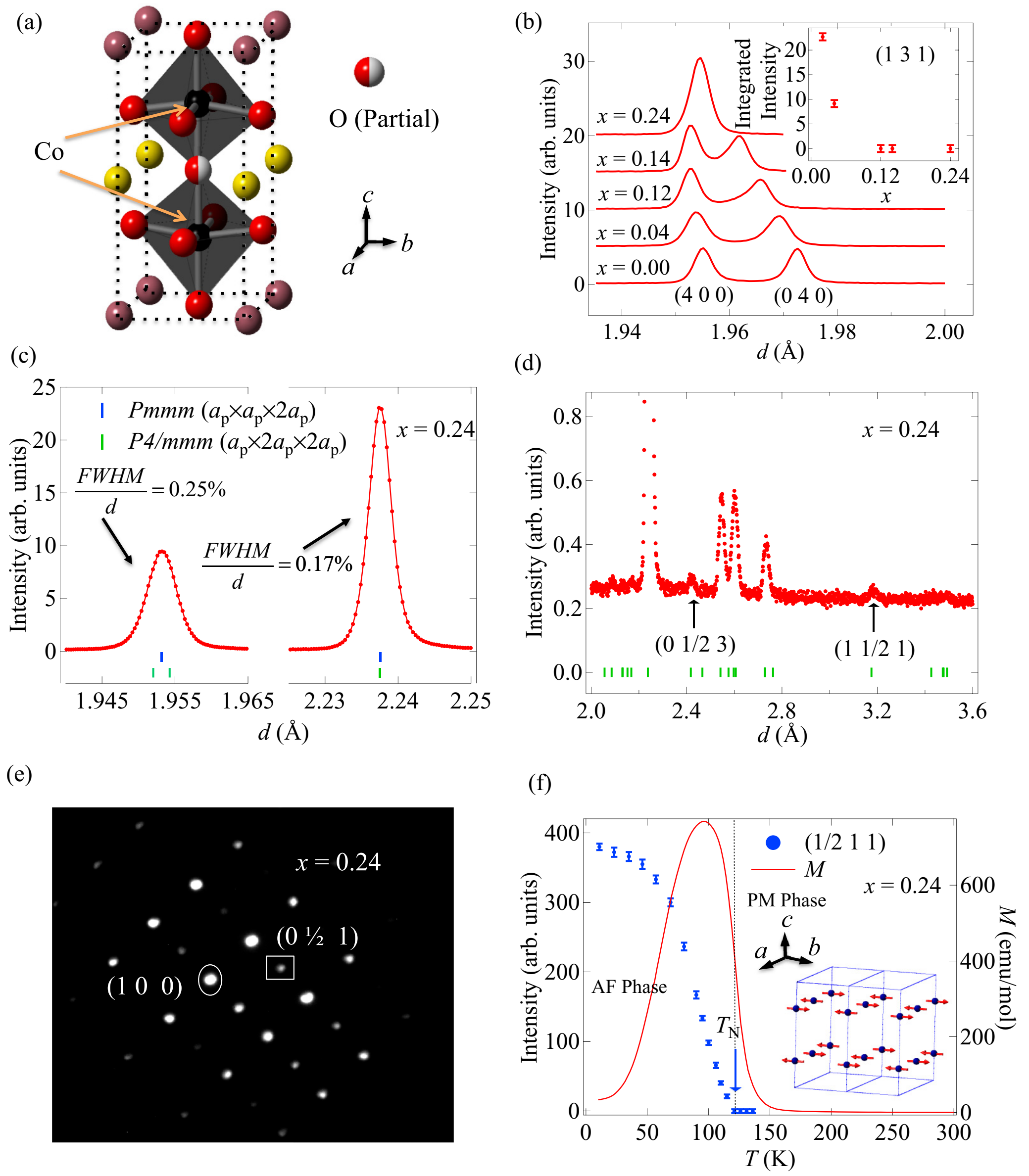

FIG. 4. (a) Crystal structure model, (b)–(d), (f) results of pulsed neutron powder diffraction, (e) electron diffraction and inverse magnetic susceptibility for $\mathrm{PrBaCo_2O_{5.5+\mathit{x}}}$ (HDI-MIT). (a) The $P4/mmm(a_p \times a_p \times 2a_p)$ unit cell with the random distribution of oxygen vacancies in the PrO_x layer, leading to only one nonequivalent crystallographic Co site. (b) The diffraction pattern of the reflections 400 and 040, as well as the integrated intensity of reflection 131 (inset), which are indexed by the unit cell $(2a_p \times 2a_p \times 2a_p)$, as a function of hole-doping fractions x at 300 K. The results suggest that the crystal structure transforms from the orthorhombic $Pmma(2a_p \times 2a_p \times 2a_p)$ to the orthorhombic $Pmmm(a_p \times 2a_p \times 2a_p)$ at $x = 0.12$. (c) Comparison of the 200 reflection (left) with the 112 reflection (right) indexed by the tetragonal $(a_p \times a_p \times 2a_p)$ unit cell. The 200 reflection splits into two reflections, whereas the 112 reflection remains single in the framework of the orthorhombic $(a_p \times 2a_p \times 2a_p)$ unit cell. (d), (e) The superlattice reflections with respect to the $(a_p \times a_p \times 2a_p)$ unit cell observed in both neutron and electron diffraction patterns of $x = 0.24$ sample at 300 K. (f) Magnetization (right axis) and integrated intensity (left axis) for the magnetic reflection $\frac{1}{2}11$ indexed by the unit cell $(a_p \times 2a_p \times 2a_p)$ as a function of temperature for $x = 0.24$, marking the antiferromagnetic phase (AF phase) with $T_N = 120$ K. The susceptibility was measured in the 100 Oe field after zero-field cooling (ZFC).

a spin-state order-disorder transition, which is in the same manner as increasing the temperature in $\mathrm{PrBaCo_2O_{5.5}}$.

D. Soft-x-ray absorption spectroscopy on both metal-insulator transitions

The common behavior of the two MITs also appears in the spectra of oxygen K-edge soft-x-ray absorption spectroscopy (XAS); see Figs. 6(a) and 6(b). The shaded region from 529 to 534 eV is due to the transition from the O 1s core level to the O 2p orbitals that are hybridized with the unoccupied Co 3d t_{2g} and e_g states, reflecting the density of states of the bottom of the conduction band. The broad structures above 534 eV are due to Ba 3d-, Co 4s-, and Pr 4f-related bands [48]. Upon decreasing either the temperature or hole-doping fraction, the threshold of spectra shifts to the higher-energy side as shown

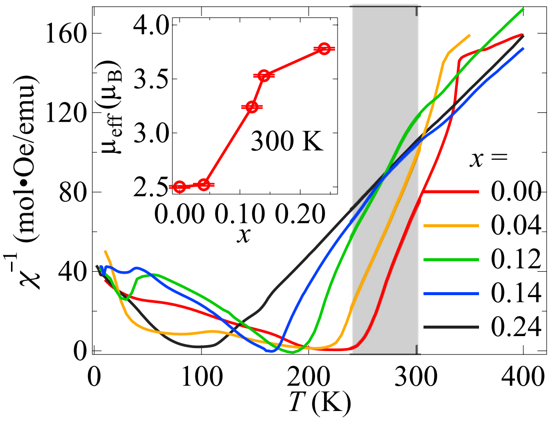

FIG. 5. Inverse magnetic susceptibility χ^{-1} as a function of temperature for various hole-doping fractions x. The susceptibilities were measured in the 100 Oe field after zero-field cooling (ZFC). The slope increases in the paramagnetic phase (shaded region) with increasing x, corresponding to the x dependence of effective magnetic moments μ_{eff} at 300 K as obtained from a Curie–Weiss fit within the shaded region (see inset).

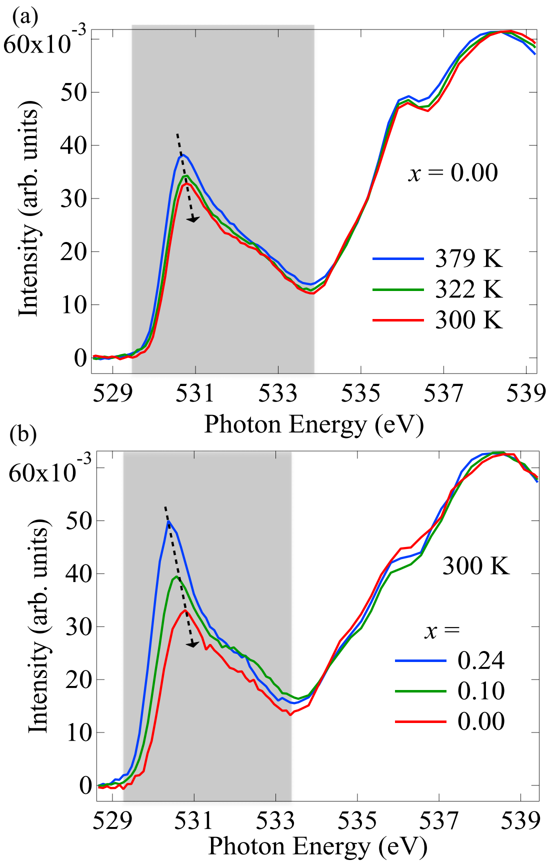

FIG. 6. (a) Soft-x-ray absorption spectra (XAS) at oxygen K edge for $PrBaCo_2O_{5.5}$ (TI-MIT) and (b) for $PrBaCo_2O_{5.5+x}$ (HDI-MIT). The intensities are normalized at about 539 eV after subtracting a small constant background. Upon decreasing either the temperature or hole-doping fraction, the threshold of the spectra shifts to the higher-energy side as shown by the arrow in the shaded region, indicating the common nature for both TI- and HDI-MITs.

by the arrows in Figs. 6(a) and 6(b), which indicates that the band gap widens for both MITs. The hole-doping dependence of spectra is analogous to that of $La_{1-x}Sr_xCoO_3$, where a part of the holes were found to reside on the O atoms, reflecting a strong Co-O hybridization [46,47]. Therefore, the shift of the absorption edge in $PrBaCo_2O_{5.5+x}$ indicates that either temperature or hole doping causes the variation in the Co-O hybridization. Consequently, a change in the strength of crystal field on Co^{3+} ions occurs, which serves as the driven force for the spin-state transition.

IV. DISCUSSION

The first discovery of the present study is that hole doping of the stoichiometric compound $PrBaCo_2O_{5.5}$ induces melting of SSO, coinciding with the insulator-metal transition. The melting of SSO triggers the crystal structure change from $Pmma(2a_p \times 2a_p \times 2a_p)$ to $Pmmm(a_p \times 2a_p \times 2a_p)$, which is identical to what occurs in the TI-MIT. Because $Pmma(2a_p \times 2a_p \times 2a_p)$ belongs to the maximal subgroup of $Pmmm(a_p \times 2a_p \times 2a_p)$, the symmetry breaking near the phase-transition point (at T_{MI} or x_{MI}) suggests that the electronic structure changes. Such electronic change manifests itself in somewhat identical manner regardless of whether it is driven by tuning temperature or hole doping: a rapid drop in resistivity in the PM phase, a rise of the effective magnetic moments, and a shift in the soft-x-ray absorption edges.

The combined results are depicted in Fig. 7, which shows a schematic phase diagram at the high-temperature regions (i.e., the PM phase) for the $PrBaCo_2O_{5.5+x}$ system. Although the data are insufficient to fully characterize the exact phase boundary, the overall picture is consistent with all the experimental data from studies of structural refinements, magnetic and transport properties, and electronic band structure. The results demonstrate that the uniform IS distribution (or HS-LS mixture) in the metallic $Pmmm(a_p \times 2a_p \times 2a_p)$ phase transforms to the SSO distribution in the insulating $Pmma(2a_p \times 2a_p \times 2a_p)$ phase. The SSO configuration consists of the HS state for Co1(Pyr), the IS state for Co2(Pyr) and Co4(Oct), and the LS state for Co3(Oct); alternatively, it is composed of HS-LS mixed states with different ratios of HS to LS among the four sites. The SSDF stems from the competition between the crystal field and Hund coupling, which in case of cobaltite are associated with the hybridization of the Co 3d with the O 2p orbitals. So the symmetry breaking of the lattice leads to different local Co-O hybridizations, which results in the SSO in $PrBaCo_2O_{5.5+x}$. Here, we argue that the Co-O hybridization is the primary factor responsible for the MITs, whereas the magnetic Co-Co direct exchange and Co-O-Co superexchange interactions are secondary. This explains why the TI-MIT occurs above the magnetic ordering temperature and why SSO is preserved even in the PM phase. The corroborative evidence for the strong Co-O hybridization is also found in the high epitaxial thin films of $LaBaCo_2O_{5.5+x}$, where the interface strain significantly alters the electronic transport properties [49–51].

Recently, some first-principle calculations [3–5] indicate that the Fe-L (L = ligand) hybridization in iron-based superconductors induces a superposition of different spin states of Fe^{2+} ions. The weight of each spin sate is modulated by this Fe-L hybridization, which can account for the unusual

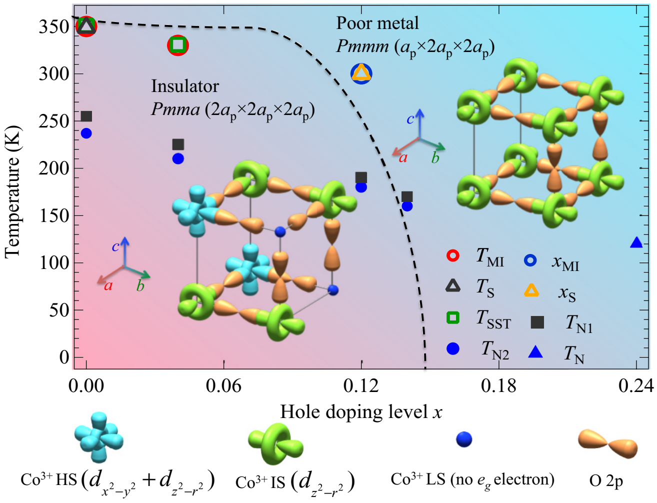

FIG. 7. Phase diagram of PrBaCo$_2$O$_{5.5+x}$ featuring the common nature for both the temperature- and hole-doping-induced MITs. The MITs are parametrized by T_{MI} and x_{MI}, which are determined from the resistivity measurements [see Fig. 2(b)]. The crystal structure transition temperatures T_S and hole-doping fractions x_S are determined by various diffraction technique probes [see Figs. 8(b) and 4(b), respectively]. T_{SST} corresponds to the SST, which is identified by the change in the slope of the inverse susceptibility vs temperature [see Fig. 5]. T_{N1}, T_{N2}, and T_N, which are determined from magnetization measurements [see Fig. 5] and neutron-diffraction measurements [see Figs. 8(e) and 4(f)], denote the magnetic-ordering transition temperature in the insulating phase and the poor-metallic phase, respectively. The schematic electronic structures are arranged in the form of a pseudocubic perovskite subcell with a Pr ion at body center. It represents the entire electronic structure because this subcell shares the CoO layer with that of the Ba-ion body center. The spin states of Co^{3+} ions are denoted by the occupancy of e_g orbital, which clearly illustrates the SSO along the a axis in the insulating phase. The pure spin state at each Co site may also be interpreted by the HS-LS mixed state with different ratios of HS to LS among the Co sites. The orbital orientations are inferred by comparing the individual Co–O bond lengths along the a, b, c axes. Thus, these orientations involve some uncertainty.

temperature dependence of the PM susceptibility [52–54]. Comparatively, our results demonstrate a different form of spatial spin-state distribution (i.e., SSO) through the complex Co-O hybridization, which also leads to the unusual temperature dependence of PM susceptibility. Therefore, we expect that SSO may occur in other systems with SSDFs, including iron-based superconductors, and it can correlate with many novel magnetic and transport properties.

V. CONCLUSION

In conclusion, we present convincing evidence from multiple probes (neutron, electron, and x-rays) that hole doping of PrBaCo$_2$O$_{5.5}$ melts the spin-state ordering (SSO) of Co^{3+} ions in conjunction with an insulator-metal transition, which is in the same manner as the temperature-induced metal-insulator transition (MIT). A unified mechanism is proposed to dominate the temperature- and hole-doping-induced MITs in the PrBaCo$_2$O$_{5.5+x}$ system, i.e., symmetry breaking coupled with SSO.

TABLE II. The atomic occupancy, coordinates, and the isotropic displacement parameters for $x = 0$ sample obtained from Rietveld refinement on neutron powder diffraction data at 300 K. The refinement is performed by using the orthorhombic $Pmma(2a_p \times 2a_p \times 2a_p)$ structure. The lattice parameters and criteria of the refinement quality are $a = 7.81837(3)$ Å, $b = 7.88788(3)$ Å, $c = 7.60990(2)$ Å; $R_{wp} = 8.70\%$.

Atom	Site	Occupancy	x	y	z	$100U_{iso}$(Å^2)
Ba	4g	1	0	0.2499(1)	0	0.28(1)
Pr	4h	1	0	0.2706(1)	0.5	0.69(1)
Co1	2e	1	0.25	0	0.2502(3)	0.66(4)
Co2	2e	1	0.75	0	0.2511(3)	0.33(4)
Co3	2f	1	0.25	0.5	0.2516(3)	0.15(4)
Co4	2f	1	0.75	0.5	0.2495(3)	0.89(5)
O1	2e	1	0.25	0	0.9994(2)	1.37(1)
O2	2f	1	0.25	0.5	0.9970(2)	0.38(1)
O3	4i	1	0.0111(1)	0	0.3059(1)	1.02(1)
O4	4k	1	0.25	0.7684(1)	0.7071(1)	0.79(1)
O5	4k	1	0.25	0.2495(1)	0.2792(1)	0.75(1)
O6	4j	1	0.0039(1)	0.5	0.2663(1)	0.82(1)
O7	2f	0.921(2)	0.25	0.5	0.5002(2)	0.43(2)
O8	2e	1	0.25	0	0.4996(12)	0.43(2)

ACKNOWLEDGMENTS

The whole study was financed by High Energy Accelerator Research Organization (KEK). The neutron diffraction experiments were carried out under the S-type project (Proposal No. 2014S05), and XAS experiments under Proposal No. 2014V001 of the Institute of Materials Structure Science, KEK. We thank Professor Y. Noda and Dr. J. Zhang for helpful discussions. We also thank M. Ishikado, T. Moyoshi, M. Shioya, and T. Muroya for their assistance with the experiments.

APPENDIX A: DETAILS OF CRYSTAL AND MAGNETIC STRUCTURE OF PrBaCo$_2$O$_{5.5}$

The TI-MIT in PrBaCo$_2$O$_{5.5}$ is identified as a first-order phase transition by both the specific-heat measurement [Fig. 8(a)] and high-resolution neutron powder diffraction (NPD) [Fig. 8(b)]. The high-resolution NPD also allows us to obtain a sufficiently high signal-to-noise ratio to detect the superlattice reflections ($\frac{3}{2}11$, $\frac{1}{2}31$, and $\frac{3}{2}01$) in the insulating phase [see Fig. 8(d)]. Furthermore, electron diffraction, a sensitive technique to detect weak superlattice reflections, also provides corroborative evidence, as shown in Fig. 8(c). These results confirm that a crystal structure phase transition occurs coincident with the TI-MIT in the PrBaCo$_2$O$_{5.5}$; specifically, it changes from high-temperature $Pmmm(a_p \times 2a_p \times 2a_p)$ to low-temperature $Pmma(2a_p \times 2a_p \times 2a_p)$. The results from Rietveld refinement for the $Pmma$ and $Pmmm$ structures are shown in Tables II and III, respectively.

The occurrence of TI-MIT in the PM phase makes it difficult to determine individual magnetic moments with neutron diffraction. Thus, we turned to lower temperatures and studied the magnetic structure in order to infer the magnetic moments in the PM phase from the nearby magnetic-ordered phase [see Fig. 3(a)]. Upon cooling the sample, a long-range magnetic

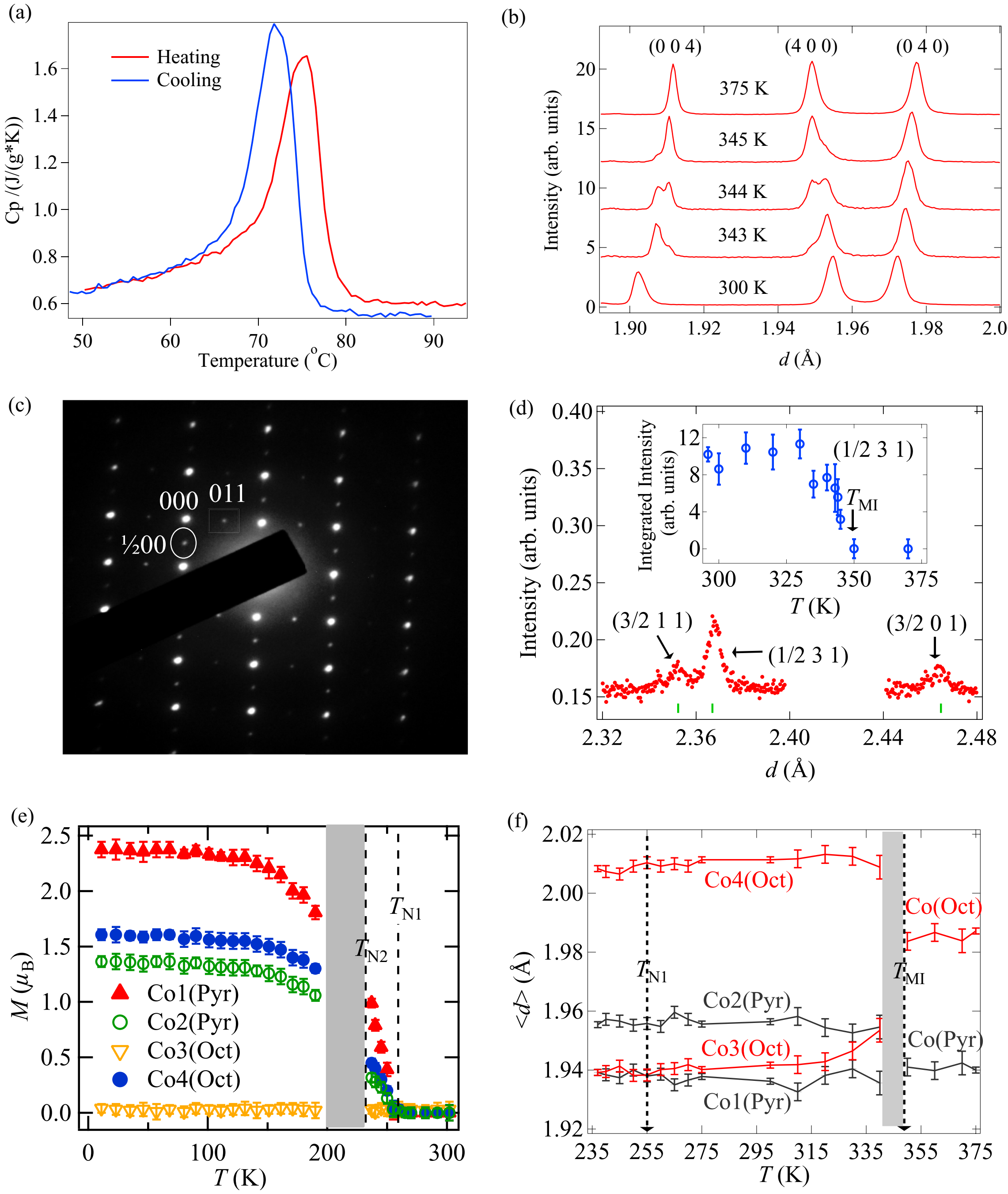

FIG. 8. Results of (a) specific heat, (c) electron diffraction, and (b), (d)–(f) pulsed neutron powder diffraction for $PrBaCo_2O_{5.5}$ (TI-MIT). (a) Specific-heat curve in both heating and cooling process. The sharp peak and hysteresis between the heating and cooling processes indicate a first-order phase transition. (b) High-resolution neutron powder diffraction pattern, where the Bragg peaks are indexed by the $(2a_p \times 2a_p \times 2a_p)$ unit cell. The coexistence of two phases in the critical region is a clear indication of a first-order phase transition. (c) Electron diffraction pattern at 300 K, which shows a superlattice reflection along the a axis with respect to the $(a_p \times 2a_p \times 2a_p)$ unit cell; i.e., the 011 reflection is the spot in the rectangle and the $\frac{1}{2}00$ reflection is the spot in the circle. We verified that no multiple scattering occurred during the measurement. (d) The superlattice reflections $\frac{3}{2}11$, $\frac{1}{2}31$, and $\frac{3}{2}01$ indexed by the $(a_p \times 2a_p \times 2a_p)$ unit cell observed by neutron powder diffraction at 300 K (below T_{MI}). (e) Magnitude of magnetic moment as a function of temperature for each Co site in phase 1, as determined from Rietveld refinement with the magnetic model in Fig. 3(b). The shaded region corresponds to the coexisting ferrimagnetic and antiferromagnetic structures. (f) Average Co–O bond length $\langle d \rangle$ as a function of temperature for each Co site in the insulating phase (below T_{MI}) of the $Pmma$ structure and in the poor-metallic phase (above T_{MI}) of the $Pmmm$ structure. The shaded region corresponds to the coexisting structures [see panel (b)]. The red (black) curves stands for CoO_6 octahedron (CoO_5 pyramid).

TABLE III. The atomic occupancy, coordinates, and the isotropic displacement parameters for the $x = 0$ sample obtained from Rietveld refinement on neutron powder diffraction data at 395 K. The refinement is performed by using the orthorhombic $Pmmm(a_p \times 2a_p \times 2a_p)$ structure. The lattice parameters and criteria of the refinement quality are $a = 3.89832(1)$ Å, b=7.90892(2) Å, c=7.64649(2) Å; R_{wp}=9.54%.

Atom	Site	Occupancy	x	y	z	$100U_{iso}$(Å^2)
Ba	$2o$	1	0.5	0.2485(1))	0	0.63(2)
Pr	$2p$	1	0.5	0.2680(1)	0.5	1.45(3)
Co1	$2r$	1	0	0.5	0.2502(2)	0.94(4)
Co2	$2q$	1	0	0	0.2513(2)	0.75(3)
O1	$1a$	1	0	0	0	1.63(3)
O2	$1e$	1	0	0.5	0	0.95(3)
O3	$1g$	0.912(3)	0	0.5	0.5	0.94(4)
O4	$1c$	0.142(3)	0	0	0.5	0.94(4)
O5	$2s$	1	0.5	0	0.3041(1)	1.79(2)
O6	$2t$	1	0.5	0.5	0.2653(1)	1.46(2)
O7	$4u$	1	0	0.2373(1)	0.2876(1)	1.45(2)

ordering emerges starting at $T_{N1} = 255$ K, which is identified by the reflection (111). This phase is henceforth referred to as phase 1 and has the magnetic propagation vector $\boldsymbol{k}_{m1} = (0,0,0)$. A new magnetic reflection $(11\frac{1}{2})$ appears starting at $T_{N2} = 237$ K, which puts in evidence a second magnetic-ordered phase. It is referred to as phase 2 and has $\boldsymbol{k}_{m2} = (0,0,\frac{1}{2})$. Since the Pr^{3+} spins become ordered below 20 K [55], the contribution to magnetic reflections only comes from the Co^{3+} spins. The temperature dependence of these reflections form a pattern analogous to those from $R\mathrm{BaCo_2O_{5.5}}$ (R = Nd [22], Gd [23], Tb [24], Dy [25], Ho [26], and Y [27]), where phase 1 has been identified as a ferrimagnetic structure with nonzero net magnetic moment and phase 2 as a antiferromagnetic structure with zero net magnetic moment. We adopted the ferromagnetic structure as the initial model in the Rietveld refinement and obtained the magnetic moments for the four sites, as shown in Fig. 3(b). As for phase 2, an antiferromagnetic structure for phase 2 can be constructed from the ferrimagnetic magnetic structure in phase 1 by reversing the magnetic moments in the neighboring Co layers linked by the Pr layer along the c axis [see Fig. 3(b)], which has been suggested by Plakhty *et al.* [24]. The relative difference in the magnitudes of moments [see Fig. 8(e)] indicates the spin-state configuration of the HS state for Co1(Pyr), the IS state for Co2(Pyr) and Co4(Oct), and the LS state for Co3(Oct). Another possible interpretation for the different moments is the spin-state disproportionation; namely, each Co site resides in a HS-LS mixed state and the ratio of HS to LS differs among the four sites.

The pronounced difference between the Shannon effective ionic radii [56] of the LS Co_{3+} ion (0.545 Å) and the HS ion (0.61 Å) in octahedron coordination also helps to identify the spin states. Figure 8(f) shows that the average Co3(Oct)–O and Co4(Oct)–O bond lengths below T_{MI} amount to a greater than 0.06 difference, consistently corroborating the conclusion that Co4(Oct) resides in the IS (the IS state has an effective ionic radii between that of the LS and HS states) or HS-LS mixed spin state whereas Co3(Oct) resides in the LS state. Therefore, a long-range SSO is identified in the $Pmma$ phase of $\mathrm{PrBaCo_2O_{5.5}}$, which has also been found in other rare-earth families, $R\mathrm{BaCo_2O_{5.5}}$ (R = Nd [22], Gd [23], Tb [24], Dy [25], Ho [26], and Y [27–29]). We could not directly determine the spin-state configuration in the high-temperature $Pmmm$ phase from the magnetic structure analysis because there is no magnetic-ordered phase nearby in phase space. However, an abrupt change in average Co–O bond length across the T_{MI} [see Fig. 8(f)] indicates the transition of spin states. Such a phenomenon has been found in $\mathrm{La_{1-x}Sr_xCoO_3}$ [57], in which the Co–O bond length of $\mathrm{La_{0.7}Sr_{0.3}CoO_3}$ shows little thermal expansion in the low-temperature ferromagnetic phase in order to retain itinerant-electron behavior; above T_c the mean equilibrium Co–O distance abruptly increases due to thermal excitation from the IS state to the HS state. In the case of $\mathrm{PrBaCo_2O_{5.5}}$, the the average Co–O bond lengths are almost temperature independent upon heating until T_{MI}, where the bond lengths undergo a discontinuous change, indicating that the constant band gap in the insulting phase closes suddenly at T_{MI} in conjunction with the Co^{3+} ions switching into different spin states. The average Co(Oct)–O bond length of the $Pmmm$ phase resides in the middle of that of the average Co3(Oct)–O and Co4(Oct)–O of the $Pmma$ phase [see Fig. 8(f)], suggesting the HS-LS or IS-LS mixed state for Co(Oct) site in $Pmmm$ phase. Similarly, the spin state of the Co(Pyr) site in the $Pmmm$ phase is inferred to be the IS state or the HS-IS mixed state because the average Co(Pyr)–O bond length is only slightly larger than that of Co1(Pyr)–O (IS) but much shorter than Co2(Pyr)–O (HS). Alternatively, the analysis of the magnetic structure of the hole-doping sample also indicates the IS or HS-LS mixed spin states in the $Pmmm$ phase. We can now understand that the crystal-structure change from $Pmma$ to $Pmmm$ corresponds to the melting of SSO.

APPENDIX B: DETAILS OF REPRESENTATION ANALYSIS AND RIETVELD REFINEMENT OF MAGNETIC STRUCTURES OF $\mathrm{PrBaCo_2O_{5.5+x}}$

The Co ions are located in two different crystallographic positions, i.e., Co1 at $2r$: [I : $(0,1/2,z)$; II : $(0,1/2,-z)$] and Co2 at $2q$: [I : $(0,0,z)$; II : $(0,0,-z)$]. The decomposition of magnetic representation using the program SARAH [41] gives the same IRs for Co1 and Co2 site, i.e.,

$$\Gamma_{Mag} = 0\Gamma_1^{(1)} + 1\Gamma_2^{(1)} + 1\Gamma_3^{(1)} + 1\Gamma_4^{(1)} + 1\Gamma_5^{(1)} + 1\Gamma_6^{(1)} + 1\Gamma_7^{(1)} + 0\Gamma_8^{(1)}. \tag{B1}$$

TABLE IV. The basis vectors (BVs) of irreducible representations (IRs) for the Co1 site at $2r$: [Atom I: $(0,\frac{1}{2},z)$; Atom II: $(0,\frac{1}{2},-z)$] of $Pmmm(a_p \times 2a_p \times 2a_p)$ crystal structure with propagation vector $\boldsymbol{k}_m = (\frac{1}{2},0,0)$. The BVs for Co2 site at $2q$: [Atom I: $(0,0,z)$; Atom II: $(0,0,-z)$] are the same as those for the Co1 site.

		Atom I			Atom II		
IR	BV	m_x	m_y	m_z	m_x	m_y	m_z
Γ_2	ϕ_1	0	0	4	0	0	−4
Γ_3	ϕ_2	4	0	0	4	0	0
Γ_4	ϕ_3	0	4	0	0	−4	0
Γ_5	ϕ_4	0	4	0	0	4	0
Γ_6	ϕ_5	4	0	0	−4	0	0
Γ_7	ϕ_6	0	0	4	0	0	4

TABLE V. Refined magnetic moments (μ_B) for the two crystallographic cobalt sites of $x = 0.24$ sample based on the basis vectors from Table IV. R_M is the magnetic R factor for Rietveld refinement.

	Γ_2	Γ_3	Γ_4	Γ_5	Γ_6	Γ_7
M_x-Co1	0	0.10(1)	0	0	1.27(1)	0
M_y-Co1	0	0	1.31(1)	0.10(1)	0	0
M_z-Co1	1.22(1)	0	0	0	0	0.44(3)
M_x-Co2	0	−0.10(1)	0	0	−1.27(1)	0
M_y-Co2	0	0	−1.31(1)	−0.10(1)	0	0
M_z-Co2	−1.22(1)	0	0	0	0	−0.44(3)
$R_M(\%)$	21.7	189.0	8.6	189.0	9.1	112.0

Also, the same BVs for both sites are obtained by means of the projection operator as given in Table IV. Through Rietveld refinement (see Table V), we find an G-type antiferromagnetic structure [see Fig. 4(f)] with the Co-ion spins pointing along either the a axis ($\Gamma 6$) or the b axis ($\Gamma 4$).

[1] N. F. Mott, Rev. Mod. Phys. **40**, 677 (1968).

[2] M. Imada, A. Fujimori, and Y. Tokura, Rev. Mod. Phys. **70**, 1039 (1998).

[3] V. Gnezdilov, Y. G. Pashkevich, P. Lemmens, D. Wulferding, T. Shevtsova, A. Gusev, D. Chareev, and A. Vasiliev, Phys. Rev. B **87**, 144508 (2013).

[4] J. Chaloupka and G. Khaliullin, Phys. Rev. Lett. **110**, 207205 (2013).

[5] Z. P. Yin, K. Haule, and G. Kotliar, Nat. Phys. **7**, 294 (2011).

[6] G. Jonker and J. V. Santen, Physica **19**, 120 (1953).

[7] P. Augustinský, V. Křápek, and J. Kuneš, Phys. Rev. Lett. **110**, 267204 (2013).

[8] N. Sundaram, Y. Jiang, I. E. Anderson, D. P. Belanger, C. H. Booth, F. Bridges, J. F. Mitchell, T. Proffen, and H. Zheng, Phys. Rev. Lett. **102**, 026401 (2009).

[9] J. B. Goodenough, J. Phys. Chem. Solids **6**, 287 (1958).

[10] P. M. Raccah and J. B. Goodenough, Phys. Rev. **155**, 932 (1967).

[11] R. Caciuffo, D. Rinaldi, G. Barucca, J. Mira, J. Rivas, M. A. Señarís-Rodríguez, P. G. Radaelli, D. Fiorani, and J. B. Goodenough, Phys. Rev. B **59**, 1068 (1999).

[12] A. M. Durand, D. P. Belanger, C. H. Booth, F. Ye, S. Chi, J. A. Fernandez-Baca, and M. Bhat, J. Phys.: Condens. Matter **25**, 382203 (2013).

[13] G. Thornton, B. Tofield, and A. Hewat, J. Solid State Chem. **61**, 301 (1986).

[14] Y. Kobayashi, T. Mitsunaga, G. Fujinawa, T. Arii, M. Suetake, K. Asai, and J. Harada, J. Phys. Soc. Jpn. **69**, 3468 (2000).

[15] M. A. Korotin, S. Y. Ezhov, I. V. Solovyev, V. I. Anisimov, D. I. Khomskii, and G. A. Sawatzky, Phys. Rev. B **54**, 5309 (1996).

[16] V. Křápek, P. Novák, J. Kuneš, D. Novoselov, D. M. Korotin, and V. I. Anisimov, Phys. Rev. B **86**, 195104 (2012).

[17] K. Knížek, Z. Jirák, J. Hejtmánek, P. Novák, and W. Ku, Phys. Rev. B **79**, 014430 (2009).

[18] J. Kuneš and V. Křápek, Phys. Rev. Lett. **106**, 256401 (2011).

[19] G. Zhang, E. Gorelov, E. Koch, and E. Pavarini, Phys. Rev. B **86**, 184413 (2012).

[20] M. W. Haverkort, Z. Hu, J. C. Cezar, T. Burnus, H. Hartmann, M. Reuther, C. Zobel, T. Lorenz, A. Tanaka, N. B. Brookes, H. H. Hsieh, H.-J. Lin, C. T. Chen, and L. H. Tjeng, Phys. Rev. Lett. **97**, 176405 (2006).

[21] A. Doi, J. Fujioka, T. Fukuda, S. Tsutsui, D. Okuyama, Y. Taguchi, T. Arima, A. Q. R. Baron, and Y. Tokura, Phys. Rev. B **90**, 081109 (2014).

[22] F. Fauth, E. Suard, V. Caignaert, and I. Mirebeau, Phys. Rev. B **66**, 184421 (2002).

[23] Y. P. Chernenkov, V. P. Plakhty, V. I. Fedorov, S. N. Barilo, S. V. Shiryaev, and G. L. Bychkov, Phys. Rev. B **71**, 184105 (2005).

[24] V. P. Plakhty, Y. P. Chernenkov, S. N. Barilo, A. Podlesnyak, E. Pomjakushina, E. V. Moskvin, and S. V. Gavrilov, Phys. Rev. B **71**, 214407 (2005).

[25] Y. Chernenkov, V. Plakhty, A. Gukasov, S. Barilo, S. Shiryaev, G. Bychkov, V. Hinkov, V. Fedorov, and V. Chekanov, Phys. Lett. A **365**, 166 (2007).

[26] J.-E. Jørgensen and L. Keller, Phys. Rev. B **77**, 024427 (2008).

[27] D. D. Khalyavin, D. N. Argyriou, U. Amann, A. A. Yaremchenko, and V. V. Kharton, Phys. Rev. B **75**, 134407 (2007).

[28] G. Aurelio, J. Curiale, R. D. Sánchez, and G. J. Cuello, Phys. Rev. B **76**, 214417 (2007).

[29] G. Aurelio, J. Curiale, R. D. Snchez, and G. J. Cuello, J. Phys.: Condens. Matter **21**, 326002 (2009).

[30] A. Maignan, C. Martin, D. Pelloquin, N. Nguyen, and B. Raveau, J. Solid State Chem. **142**, 247 (1999).

[31] H. Kusuya, A. Machida, Y. Moritomo, K. Kato, E. Nishibori, M. Takata, M. Sakata, and A. Nakamura, J. Phys. Soc. Jpn. **70**, 3577 (2001).

[32] C. Frontera, J. L. García-Muñoz, A. Llobet, and M. A. G. Aranda, Phys. Rev. B **65**, 180405 (2002).

[33] D. Chernyshov, V. Dmitriev, E. Pomjakushina, K. Conder, M. Stingaciu, V. Pomjakushin, A. Podlesnyak, A. A. Taskin, and Y. Ando, Phys. Rev. B **78**, 024105 (2008).

[34] D. D. Khalyavin, Phys. Rev. B **72**, 134408 (2005).

[35] A. A. Taskin, A. N. Lavrov, and Y. Ando, Phys. Rev. B **71**, 134414 (2005).

[36] S. Bao, C. Ma, G. Chen, X. Xu, E. Enriquez, C. Chen, Y. Zhang, J. L. Bettis Jr., M.-H. Whangbo, C. Dong, and Q. Zhang, Sci. Rep. **4**, 4726 (2014).

[37] F. Fauth, E. Suard, V. Caignaert, B. Domengès, I. Mirebeau, and L. Keller, Eur. Phys. J. B **21**, 163 (2001).

[38] M. Soda, Y. Yasui, T. Fujita, T. Miyashita, M. Sato, and K. Kakurai, J. Phys. Soc. Jpn. **72**, 1729 (2003).

[39] K. Zhang, L. Ge, R. Ran, Z. Shao, and S. Liu, Acta Mater. **56**, 4876 (2008).

[40] G. Kim, S. Wang, A. J. Jacobson, L. Reimus, P. Brodersen, and C. A. Mims, J. Mater. Chem. **17**, 2500 (2007).

[41] A. Wills, Physica B (Amsterdam, Neth.) **278**, 680 (2000).

[42] R. Oishi, M. Yonemura, Y. Nishimaki, S. Torii, A. Hoshikawa, T. Ishigaki, T. Morishima, K. Mori, and T. Kamiyama, Nucl. Instrum. Methods Phys. Res., Sect. A **600**, 94 (2009).

[43] R. Oishi-Tomiyasu, M. Yonemura, T. Morishima, A. Hoshikawa, S. Torii, T. Ishigaki, and T. Kamiyama, J. Appl. Crystallogr. **45**, 299 (2012).

[44] J. RodrÌguez-Carvajal, Physica B (Amsterdam, Neth.) **192**, 55 (1993).

[45] C. Frontera, J. L. García-Muñoz, A. E. Carrillo, C. Ritter, D. Martín y Marero, and A. Caneiro, Phys. Rev. B **70**, 184428 (2004).

[46] S. Medling, Y. Lee, H. Zheng, J. F. Mitchell, J. W. Freeland, B. N. Harmon, and F. Bridges, Phys. Rev. Lett. **109**, 157204 (2012).

[47] S. Medling, Y. Lee, H. Zheng, J. F. Mitchell, J. W. Freeland, B. N. Harmon, and F. Bridges, Phys. Status Solidi C **10**, 254 (2013).

[48] Z. Hu, H. Wu, M. W. Haverkort, H. H. Hsieh, H. J. Lin, T. Lorenz, J. Baier, A. Reichl, I. Bonn, C. Felser, A. Tanaka, C. T. Chen, and L. H. Tjeng, Phys. Rev. Lett. **92**, 207402 (2004).

[49] C. R. Ma, M. Liu, J. Liu, G. Collins, Y. M. Zhang, H. B. Wang, C. L. Chen, Y. Lin, J. He, J. C. Jiang, E. I. Meletis, and A. J. Jacobson, ACS Appl. Mater. Interfaces **6**, 2540 (2014).

[50] C. Ma, M. Liu, G. Collins, H. Wang, S. Bao, X. Xu, E. Enriquez, C. Chen, Y. Lin, and M.-H. Whangbo, ACS Appl. Mater. Interfaces **5**, 451 (2013).

[51] M. Liu, C. Ma, J. Liu, G. Collins, C. Chen, J. He, J. Jiang, E. I. Meletis, L. Sun, A. J. Jacobson, and M.-H. Whangbo, ACS Appl. Mater. Interfaces **4**, 5524 (2012).

[52] T. Imai, K. Ahilan, F. L. Ning, T. M. McQueen, and R. J. Cava, Phys. Rev. Lett. **102**, 177005 (2009).

[53] H. Gretarsson, S. R. Saha, T. Drye, J. Paglione, J. Kim, D. Casa, T. Gog, W. Wu, S. R. Julian, and Y.-J. Kim, Phys. Rev. Lett. **110**, 047003 (2013).

[54] G. Grechnev, A. Panfilov, A. Fedorchenko, V. Desnenko, S. Gnatchenko, V. Tsurkan, J. Deisenhofer, A. Loidl, D. Chareev, O. Volkova, and A. Vasiliev, J. Magn. Magn. Mater. **324**, 3460 (2012).

[55] W.-H. Li, K. J. Chang, W. T. Hsieh, K. C. Lee, J. W. Lynn, and H. D. Yang, Phys. Rev. B **48**, 519 (1993).

[56] R. D. Shannon, Acta Crystallogr., Sect. A: Cryst. Phys., Diffr., Theor. Gen. Crystallogr. **32**, 751 (1976).

[57] R. Caciuffo, J. Mira, J. Rivas, M. A. Sears-Rodrguez, P. G. Radaelli, F. Carsughi, D. Fiorani, and J. B. Goodenough, Europhys. Lett. **45**, 399 (1999).